Helical vortices: linear stability analysis and nonlinear dynamics

C. Selçuk[1,2]**, I. Delbende**[1,3] **and M. Rossi**[4,5]

[1] LIMSI, CNRS, Université Paris-Saclay, rue John von Neumann, 91405 Orsay, France

[2] Sorbonne Universités, UPMC Univ Paris 06, IFD, 4 place Jussieu, 75252 Paris Cedex 05, France

[3] Sorbonne Universités, UPMC Univ Paris 06, UFR d'Ingénierie, 4 place Jussieu, 75252 Paris Cedex 05, France

[4] Sorbonne Universités, UPMC Univ Paris 06, UMR 7190, Institut Jean Le Rond d'Alembert, 75252 Paris Cedex 05, France

[5] CNRS, UMR 7190, Institut Jean Le Rond d'Alembert, 75252 Paris Cedex 05, France

E-mail: `can.selcuk@limsi.fr`

Abstract. We numerically investigate, within the context of helical symmetry, the dynamics of a regular array of two or three helical vortices with or without a straight central hub vortex. The Navier-Stokes equations are linearised to study the instabilities of such basic states. For vortices with low pitches, an unstable mode is extracted which corresponds to a displacement mode and growth rates are found to compare well with results valid for an infinite row of point vortices or an infinite alley of vortex rings. For larger pitches, the system is stable with respect to helically symmetric perturbations. In the nonlinear regime, we follow the time-evolution of the above basic states when initially perturbed by the dominant instability mode. For two vortices, sequences of overtaking events, leapfrogging and eventually merging are observed. The transition between such behaviours occurs at a critical ratio involving the core size and the vortex-separation distance. Cases with three helical vortices are also presented.

Keywords: Vortex, helical vortices, instability, nonlinear dynamics, numerical simulation

1. Introduction

Helical vortices are encountered in nature and numerous industrial applications. For instance, vortices characterized by a helical geometry are shed downstream of rotating blades. Such flows are the simplest prototypes in which combined effects of torsion and curvature are present. While vortices can still be geometrically described as vorticity tubes, their global motions resulting from the mutual vortex interactions are highly complex. In the past decades, a lot of efforts has been devoted to the understanding and prediction of such dynamics. Most theoretical studies used an idealised formulation: helical vortices were modelled as inviscid filaments in which the vorticity field was represented by thin curved tubes, the main problem being to deal with their singular behaviour. Among these works, some were devoted to finding equilibrium solutions and, more precisely, to characterize their angular velocity and the induced velocity [1, 2, 3, 4, 5, 6]. A few studies directly used the Euler equations to compute equilibria. In particular, Lucas and Dritschel [7] exhibited a family of equilibria with arbitrary core size using helically symmetric Euler equations. By imposing geometrical constraints on the centroid location and the vortex core size at fixed pitch, their approach managed to find helical patch solutions which were steady in some rotating frame.

The study of instabilities developing in such vortex systems was the focus of many works, mainly in the framework of the vortex-filament approach [8, 9, 10, 11, 12, 13]. Widnall [8] first predicted the linear stability features of one helical vortex with respect to sinusoidal perturbations. Three types of instability modes were found: a long wavelength mode, a mutual-inductance mode and a short wavelength mode. Gupta and Loewy [9] later extended this work to a regular array of helical vortices: modes analogous to those obtained for one single vortex were found, as well as additional modes arising from the interaction between distinct vortices. Okulov [10] focused specifically on the helically symmetric modes in an array of N vortices with circular cores. It was shown that such systems were unstable when the helical pitch was smaller than a threshold value. Later, Okulov and Sørensen [11] investigated the effect of a central hub vortex, as in rotor wakes: the central hub was always destabilizing.

Helical vortices were also experimentally studied. For instance, Felli *et al.*[14] studied the spatial development of marine propeller wakes for two to four blades: the growth of perturbations led to vortex groupings and eventually dissipation of the coherent structures. This study revealed the presence, at the axis, of the hub vortex playing a role on the instability process. Bolnot *et al.* [15, 16], and Quaranta *et al.* [17] used a water channel in which one- and two-bladed rotors generated carefully monitored helical wakes. Instability modes were forced by modulating the rotor angular velocity or by a small asymmetry between the two blades. The temporal growth rates measured as a function of the imposed wavelength were found to agree with the filamentary theory. In experiments, it is difficult though to cover large ranges of helical pitches, core sizes and Reynolds numbers. This can be performed more easily using a numerical approach. Performing a parametric study in order to find the stability thresholds is one goal of the present numerical work. Concerning basic flows, existing results in the inviscid domain are mainly obtained via vortex filaments which approximate the Euler dynamics. The present approach extends the semi-analytical studies to the viscous framework and gives access to the velocity structure inside vortex cores. For linear instability, the results we obtain are shown below to be close to vortex filament theory. This analysis permits to reach the inner structure of the unstable modes though it remains simple here. More importantly, it computes the nonlinear evolution within the helical framework. Indeed our approach introduces diffusion which is important in the nonlinear evolution towards merging, as it is for two-dimensional vortex pairing.

This article focuses on vortices with imposed helical symmetry. Thanks to this invariance, the problem is reduced to a two-dimensional one still preserving fundamental three-dimensional effects (curvature and torsion). This simplification allows for simulations at higher Reynolds numbers than in a complete three-dimensional simulation. Such an approach filters out ingredients such as wake spatial development, fluid-rotor interaction and turbulence. On the contrary it focuses on the fundamental physical mechanisms (induction and diffusion). A numerical code called HELIX has been developed at LIMSI-CNRS and d'Alembert-UPMC [18] to implement the helical formulation of the incompressible Navier-Stokes equations: it is quasi-two dimensional, based on pseudo-spectral and finite-difference methods along the azimuthal and radial directions, respectively. This code is used to determine basic states with prescribed characteristics (core size, helical pitch, helix radius). A linearised version of this code coupled to an Arnoldi algorithm enables one to perform the linear stability analysis and to extract dominant modes. The nonlinear evolutions of such modes are then computed within the helical framework.

2. Helical framework and governing equations

Linear and nonlinear instabilities of jets, wakes or boundary layers, are often studied in the framework of a parallel flow approximation. A similar local hypothesis can be used for rotor wakes: the base flow may be assumed to satisfy helical symmetry. A flow is helically symmetric if it remains invariant through the combined action of a translation of arbitrary magnitude H along a given axis and of a rotation of angle $\theta_s = H/L$ around the same axis (see figure 1-a) where $2\pi L$ is the *helix pitch*. The sign of L defines the direction of the helix: $L > 0$ corresponds to a right-handed helix and $L < 0$ to a left-handed one.

In the context of helical symmetry, it is convenient to introduce variable $\varphi = \theta - z/L$ and a new orthonormal basis $(\boldsymbol{e_B}, \boldsymbol{e_r}, \boldsymbol{e_\varphi})$ based on the standard cylindrical basis $(\boldsymbol{e_r}, \boldsymbol{e_\theta}, \boldsymbol{e_z})$ (see figure 1-b). The Beltrami vector $\boldsymbol{e_B}$ is a unit vector locally tangent to the helical lines $\varphi = cst$:

$$\boldsymbol{e_B} = \alpha\left(r\right)\left(\boldsymbol{e_z} + \frac{r}{L}\boldsymbol{e_\theta}\right) \qquad \text{with} \qquad \alpha(r) = \left(1 + \frac{r^2}{L^2}\right)^{-1/2}. \tag{1}$$

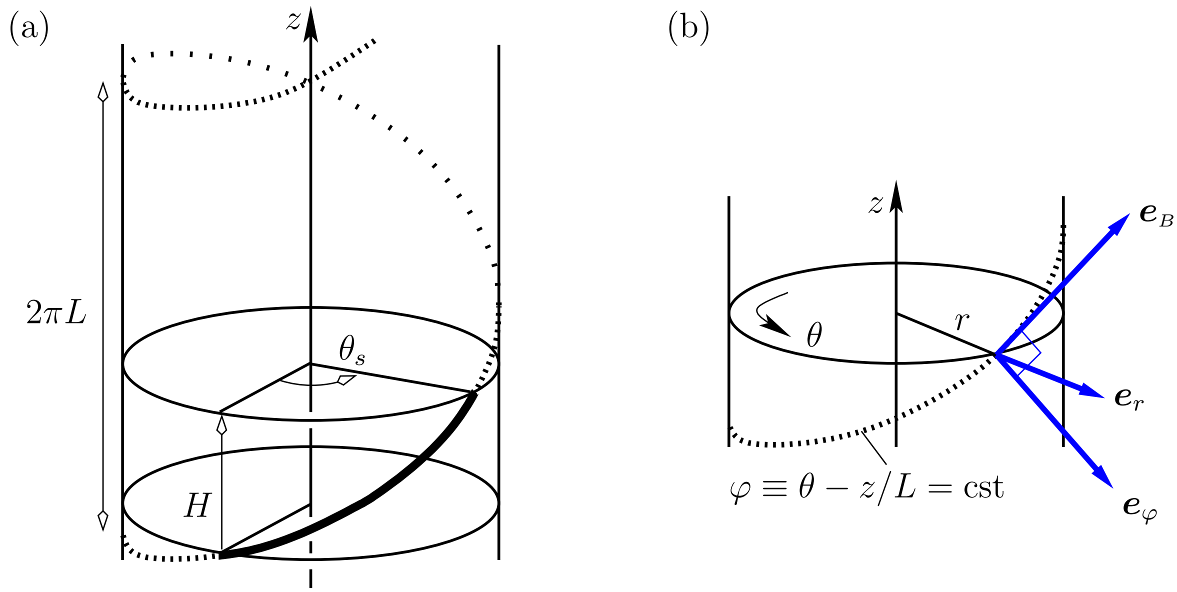

Figure 1: (a) Geometrical parameters defining helical symmetry. (b) Local orthonormal *helical* basis $(\boldsymbol{e_r}, \boldsymbol{e_B}, \boldsymbol{e_\varphi})$.

The third unit vector $\boldsymbol{e_\varphi}$ is given by

$$\boldsymbol{e_\varphi} = \boldsymbol{e_B} \times \boldsymbol{e_r} = \alpha(r)\left(\boldsymbol{e_\theta} - \frac{z}{L}\boldsymbol{e_z}\right). \tag{2}$$

Consequently, any velocity field can be expressed as $\boldsymbol{u} = u_r\,\boldsymbol{e_r} + u_B\,\boldsymbol{e_B} + u_\varphi\,\boldsymbol{e_\varphi}$ with

$$u_B(r,\theta,z) = \boldsymbol{u}\cdot\boldsymbol{e_B} = \alpha(r)\left(u_z + \frac{r}{L}u_\theta\right) \tag{3}$$

$$u_\varphi(r,\theta,z) = \boldsymbol{u}\cdot\boldsymbol{e_\varphi} = \alpha(r)\left(u_\theta - \frac{r}{L}u_z\right). \tag{4}$$

For helically symmetric flows, components u_r, u_B, u_φ are constant along the helical lines

$$\boldsymbol{e_B}\cdot\boldsymbol{\nabla}u_r = \boldsymbol{e_B}\cdot\boldsymbol{\nabla}u_B = \boldsymbol{e_B}\cdot\boldsymbol{\nabla}u_\varphi = 0, \tag{5}$$

or equivalently, they depend on only two variables (r,φ). A helically symmetric velocity field $\boldsymbol{u}$ is thus given by

$$\boldsymbol{u} = u_r(r,\varphi,t)\;\boldsymbol{e_r}(\theta) + u_B(r,\varphi,t)\;\boldsymbol{e_B}(r,\theta) + u_\varphi(r,\varphi,t)\;\boldsymbol{e_\varphi}(r,\theta). \tag{6}$$

For incompressible and helically symmetric flows, the divergenceless character of both velocity and vorticity is automatically ensured by introducing the helical components of velocity $u_B(r,\varphi,t)$ and vorticity $\omega_B(r,\varphi,t)$ as well as the streamfunction $\Psi(r,\varphi,t)$ so that

$$\boldsymbol{u}(r,\varphi,t) = u_B(r,\varphi,t)\,\boldsymbol{e_B} + \alpha(r)\boldsymbol{\nabla}\Psi(r,\varphi,t)\times\boldsymbol{e_B}, \tag{7}$$

$$\boldsymbol{\omega}(r,\varphi,t) = \omega_B(r,\varphi,t)\,\boldsymbol{e_B} + \alpha(r)\boldsymbol{\nabla}\left(\frac{u_B(r,\varphi,t)}{\alpha}\right)\times\boldsymbol{e_B}. \tag{8}$$

In addition, fields u_B, ω_B and Ψ are related *via* a generalised $\Psi - \omega_B$ relationship:

$$\omega_B = -\mathbb{L}\,\Psi + 2\frac{\alpha^2}{L}u_B \tag{9}$$

where $\mathbb{L}$ stands for the modified Laplace operator:

$$\mathbb{L}\,(.) \equiv \frac{1}{r\alpha}\frac{\partial}{\partial r}\left(r\alpha^2\frac{\partial}{\partial r}\,(.)\right) + \frac{1}{r^2\alpha}\frac{\partial^2}{\partial\varphi^2}\,(.)\,. \tag{10}$$

In this representation, the dynamics is fully described by two equations coupling u_B and ω_B:

$$\frac{\partial}{\partial t}u_B + \mathcal{NL}_u = \mathcal{VT}_u \tag{11}$$

$$\frac{\partial}{\partial t}\omega_B + \mathcal{NL}_\omega = \mathcal{VT}_\omega \tag{12}$$

The nonlinear terms are given by

$$\mathcal{NL}_u \equiv \boldsymbol{e}_B \cdot (\boldsymbol{\omega} \times \boldsymbol{u})\,, \tag{13}$$

$$\begin{aligned}\mathcal{NL}_\omega &\equiv \boldsymbol{e}_B \cdot \boldsymbol{\nabla} \times (\boldsymbol{\omega} \times \boldsymbol{u})\,, \\ &= \frac{1}{r\alpha}\left\{\frac{\partial}{\partial r}\,(r\alpha g_\varphi) - \frac{\partial}{\partial\varphi}g_r\right\} + \frac{2\alpha^2}{L}g_B + \frac{\alpha}{L^2}\frac{\partial}{\partial\varphi}\left(u_B^2\right)\end{aligned} \tag{14}$$

with

$$g_\varphi = \omega_B\,u_r, \quad g_r = -\omega_B\,u_\varphi, \quad g_B = \omega_r\,u_\varphi - \omega_\varphi\,u_r,$$

and the viscous terms

$$\mathcal{VT}_u \equiv \nu\left[\mathbb{L}\left(\frac{u_B}{\alpha}\right) - \frac{2\alpha^2}{L}\omega_B\right], \tag{15}$$

$$\begin{aligned}\mathcal{VT}_\omega &\equiv -\nu\;\boldsymbol{e}_B \cdot \boldsymbol{\nabla} \times [\boldsymbol{\nabla} \times \boldsymbol{\omega}] \\ &= \nu\;\left[\mathbb{L}\left(\frac{\omega_B}{\alpha}\right) - \left(\frac{2\alpha^2}{L}\right)^2\omega_B\right] + \nu\,\frac{2\alpha^2}{L}\mathbb{L}\left(\frac{u_B}{\alpha}\right).\end{aligned} \tag{16}$$

For $L \to \pm\infty$, helical lines tend toward straight lines and the above equations becomes the usual $\Psi - \omega$ formulation. When $L \neq \infty$, this usual dynamic is generalised and in particular, the components u_B and ω_B are coupled through the viscous terms $\mathcal{VT}_u$ and $\mathcal{VT}_\omega$.

The numerical code that implements the time advance of equations (11)–(12) is briefly described below, an extensive description can be found in Delbende *et al.* [18]. Quantities are represented as functions of r and φ. The code uses second order finite differences in the radial direction, and a decomposition over Fourier modes along the 2π-periodic direction φ. The time advance uses a second-order backward discretisation of the temporal derivative. Viscous terms are treated in a fully implicit manner while nonlinear terms are kept explicit through a second order Adams–Bashforth extrapolation. At each time step, these nonlinear terms are evaluated in physical space on a grid of n_r points along the radial direction by n_φ points along the azimuth, and are then transformed to the spectral space where a standard 2/3 dealiasing procedure is applied. The numerical domain has a typical radial extension of a few helix radii. It thus encompasses the vorticity region, so that the matching of solutions to the potential field assumed to prevail outside the domain is enforced at the outer boundary. Moreover, a condition of zero axial velocity is imposed as $r \to \infty$: this selects a specific reference frame which might differ from the laboratory frame in experiments.

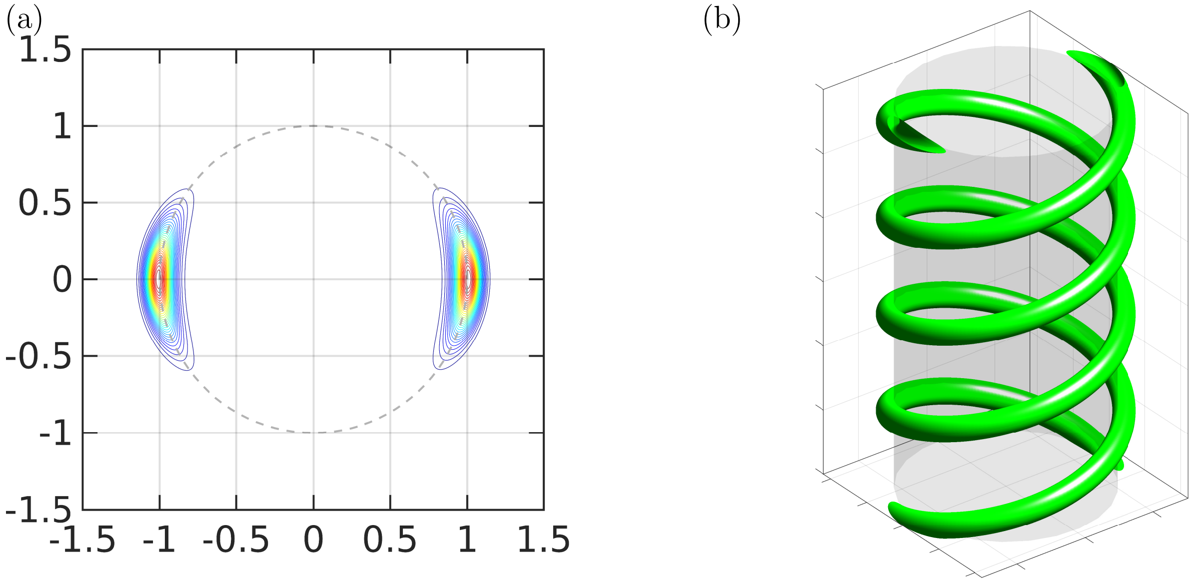

Figure 2: Two helical vortices of reduced pitch $L = 0.3$ with core size $a_b = 0.09$ (a) vorticity field ω_B in the plane orthogonal to the $z-$axis (b) Iso-vorticity surface in three-dimensional space.

3. Linear stability analysis

3.1. Basic states solutions: frozen quasi-equilibria

The stability of a regular array of N identical helical vortices of circulation Γ is here studied in the presence or absence of a straight hub vortex of circulation $-N\Gamma$ along the $z-$axis (this last configuration is akin to that of rotor wakes). In the framework of Euler dynamics, such systems would correspond to steadily rotating equilibrium states. When viscosity is present, equilibrium cannot be maintained but there exist unsteady solutions which evolve in such a way that the system remains close to such inviscid equilibria. These unsteady solutions are called quasi-equilibria: their core size $a\,(t)$, angular velocity $\Omega\,(t)$ and helix radius $r_A\,(t)$ are slowly changing in time. Quasi-equilibria are obtained by DNS starting from initial conditions which are close to singular helical filaments: after a short transient, Kelvin waves are damped and the system reaches such a basic state. These features are detailed elsewhere [19, 20]. Figure 2 illustrates such a state for an array of two vortices.

The stability analyses presented here below are performed around a basic state corresponding to a quasi-equilibrium solution at a given time t_b. This state is defined by velocity $\boldsymbol{u}(t_b)$ and vorticity $\boldsymbol{\omega}(t_b)$ in steady rotation at angular velocity $\Omega\,(t_b)$. As it is usually done in shear flow at high Reynolds numbers, the instability study of this frozen flow is pertinent since the perturbations are expected to grow faster than the timescale characterizing the action of viscous diffusion on a quasi-equilibrium. Note that this approximation is mandatory in order to use standard temporal stability techniques: in the reference frame rotating with the vortices at rate $\Omega(t_b)$, the basic state becomes indeed steady and helical components are changed as follows:

$$u_B^R = u_B - \frac{r^2}{L}\alpha\Omega(t_b), \tag{17}$$

$$u_\varphi^R = u_\varphi - r\alpha\Omega(t_b), \tag{18}$$

$$\omega_B^R = \omega_B - 2\alpha\Omega(t_b), \tag{19}$$

$$\omega_\varphi^R = \omega_\varphi + \frac{2r}{L}\alpha\Omega(t_b). \tag{20}$$

In the following discussion, all quantities are made dimensionless using $R \equiv r_A(t_b)$ as a characteristic length scale and R^2/Γ as a characteristic time scale. The Reynolds number is thus defined as $Re = \Gamma/\nu$. In dimensionless units, the numerical domain is generally the disk $r \leq 3$ and is meshed using $n_r \times n_\phi = 512 \times 384$ grid points which has been checked to ensure convergence. Typical time step at $Re = 10^4$ is $\delta t = 10^{-4}$. These values are used to compute the basic flow. The same discretisation parameters are used below for the stability equations (21)–(23) as well.

3.2. Linear stability equations

In the present paper, we restrict the general stability problem and focus on helically symmetric perturbations only. The viscous diffusion acts on the perturbations although we have neglected its action on the basic state. This is coherent with the frozen flow approximation. In the framework of helical symmetry, let us present the linearisation of equations (11) and (12). When written in the rotating frame of reference, a Coriolis force appears in the dynamical equations. The velocity perturbation u'_B satisfy

$$\begin{aligned}&\frac{\partial}{\partial t}u'_B + \omega_r^R u'_\varphi + u_\varphi^R \omega'_r - (\omega_\varphi^R u'_r + u_r^R \omega'_\varphi) + \frac{2\Omega}{L}\alpha r u'_r \\ &= \nu\left[\mathbb{L}\left(\frac{u'_B}{\alpha}\right) - 2\frac{\alpha^2}{L}\omega'_B\right],\end{aligned} \tag{21}$$

while vorticity perturbation ω'_B is governed by

$$\begin{aligned}&\frac{\partial}{\partial t}\omega'_B + \frac{1}{r\alpha}\frac{\partial}{\partial r}\left(r\alpha\left(\omega_B^R u'_r + u_r^R \omega'_B\right)\right) + \frac{1}{r\alpha}\frac{\partial}{\partial\varphi}\left(\omega_B^R u'_\varphi + u_\varphi^R \omega'_B\right) \\ &+ \frac{2\alpha^2}{L}\left[\omega_r^R u'_\varphi + u_\varphi^R \omega'_r - \left(\omega_\varphi^R u'_r + u_r^R \omega'_\varphi\right)\right] + \frac{\alpha}{L^2}\frac{\partial}{\partial\varphi}\left(2u_B^R u'_B\right) + \frac{2\Omega}{L}\frac{\partial u'_B}{\partial\varphi} \\ &= \nu\left[\mathbb{L}\left(\frac{\omega'_B}{\alpha}\right) - \left(2\frac{\alpha^2}{L}\right)^2\omega'_B\right] + \nu\frac{2\alpha^2}{L}\mathbb{L}\left(\frac{u'_B}{\alpha}\right).\end{aligned} \tag{22}$$

Following equation (10), streamfunction perturbation Ψ' is linked to ω'_B and u'_B *via*:

$$\mathbb{L}\,\Psi' = 2\frac{\alpha^2}{L}u'_B - \omega'_B. \tag{23}$$

The spatial discretisation of this system leads to

$$\frac{\partial}{\partial t}\boldsymbol{q'} = \mathbf{A}\,\boldsymbol{q'} \quad \text{with} \quad \boldsymbol{q'} = (u'_B\,, \omega'_B)^T \tag{24}$$

where $\mathbf{A}$ is a linear matrix of size $2n_p \times 2n_p$, with $n_p = n_r \times n_\varphi$. Stability features are extracted by an Arnoldi algorithm providing the leading eigenvalues λ

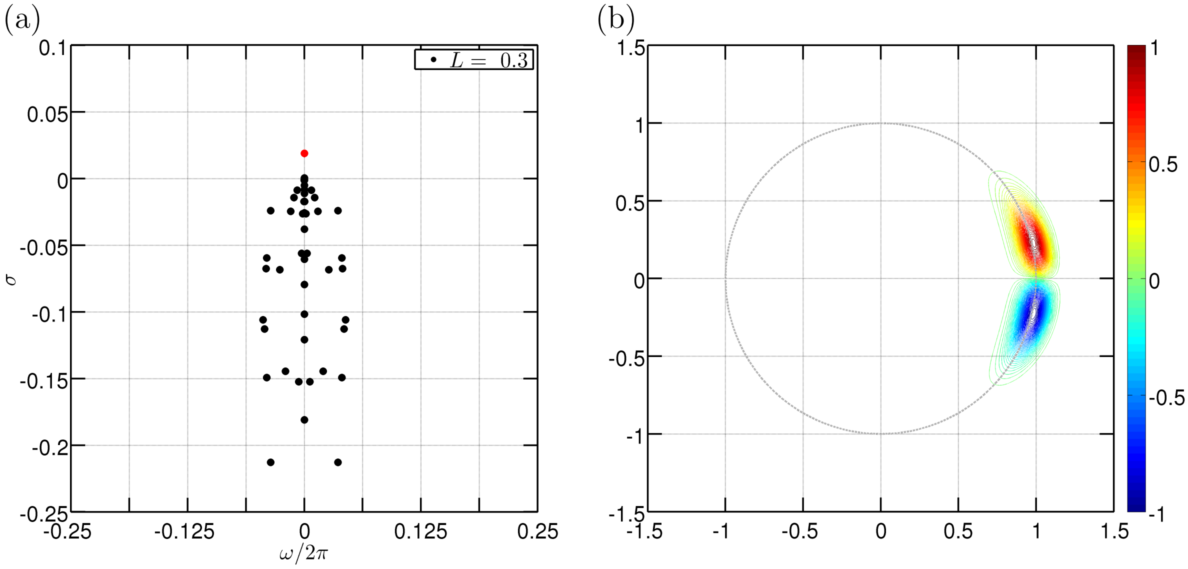

Figure 3: (a) Spectrum in the $(\omega/2\pi, \sigma)$ plane for a single helical vortex with reduced pitch $L = 0.3$ and core size $a = 0.09$ at $Re = 10000$. The 50 dominant eigenvalues are displayed. (b) Mode structure of the mode represented with a red dot in graph (a): contours of the real part of $\hat{\omega}_B$ in the plane orthogonal to the $z-$axis.

of $\mathbf{A}$ along with their associated eigenvectors $\boldsymbol{v_A}$. This method generates accurate eigenvalue approximations from an upper Hessenberg factorisation of the operator $\mathbf{A}$ [21, 22, 23]. The eigenvectors $\boldsymbol{v_A} = (\tilde{\omega}_B, \tilde{u}_B)^T$ contain a mix of helical vorticity and velocity components and are obtained up to a complex factor. In order to define these eigenvectors in a unique fashion, we search for the point (r_+, φ_+) where the maximum of vorticity $\tilde{\omega_B}$ is reached, and a normalisation is performed by applying $\hat{\omega}_B = \dfrac{\tilde{\omega}_B}{\tilde{\omega}_B\,(r_+, \varphi_+)}$, $\hat{u}_B = \dfrac{\tilde{u}_B}{\tilde{\omega}_B\,(r_+, \varphi_+)}$.

3.3. Linear stability: results for one helical vortex

We present the spectrum and neutral mode found in the stability of a single helical vortex. In figure 3-a, the stability spectrum is plotted for a single helical vortex for $L = 0.3$, $a = 0.09$ and $Re = 10000$ where only the 50 eigenvalues of largest growth rate are displayed. All modes have negative eigenvalues except one. This latter mode possesses several features: (i) it possesses a small positive real eigenvalue; (ii) the imaginary part of the associated eigenmode $\hat{\omega}_B$ is zero; (iii) the real part of $\hat{\omega}_B$ (see figure 3-b) is characterised by two lobes of opposite sign vorticity. When superimposed on the base flow, this mode induces a displacement of the whole structure in the azimuthal direction. Such a mode is present because of the invariance of the base flow with respect to rotation around the central axis. For this reason, it is also expected to be neutral and steady ($\sigma + i\omega = 0$). The Arnoldi procedure and more generally the finite numerical precision cannot lead to a perfect zero eigenvalue in this case: the very small growth

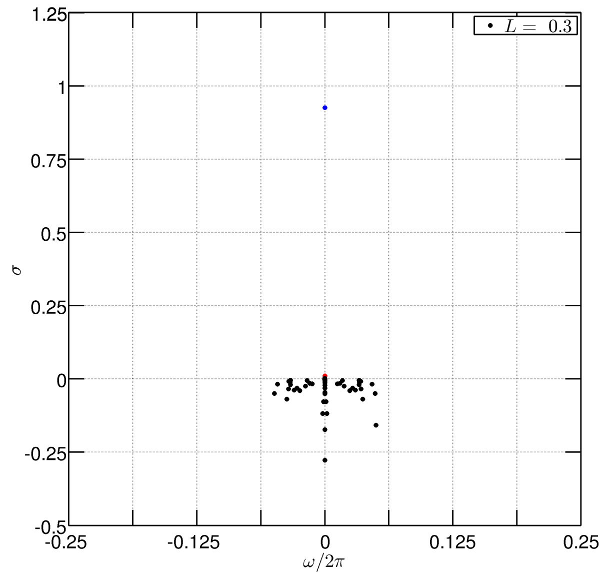

Figure 4: Spectrum in the $(\omega/2\pi, \sigma)$ plane for two helical vortices with $L = 0.3$ and $a = 0.09$ at $Re = 10000$. The first 50 eigenvalues are displayed. The dominant eigenmode is represented in blue and the neutral one in red.

rate (of order 10^{-2}) obtained here thus quantifies the accuracy of our results. In the framework of helical symmetry, one helical vortex is stable and the neutral displacement mode does not play a role.

4. Linear stability results for two helical vortices

Figure 4 displays the 50 most unstable eigenvalues for two helical vortices with $L = 0.3$, $a = 0.09$ and $Re = 10000$. A similar spectrum is obtained when parameters L, a and Re are varied. Only two modes with positive growth rates emerge: one dominant mode with growth rate $\sigma = 0.925$ as well as a marginally stable mode evaluated at $\sigma = 0.010$, both modes being stationary ($\omega = 0$). Similarly to the single vortex case, the latter mode is the neutral mode (see figure 5). In figure 6-a, the real pat of the unstable mode is represented, the associated imaginary part being zero. The mode is characterised by two lobes of opposite sign vorticity. This implies a radial inward displacement for one vortex and an outward one for its companion (see figure 6-a and the arrows in the three-dimensional representation on figure 6-b). This induced vortex motion has also an axial component. This mode structure, when visualized in the meridional (r, z) plane, is similar to a pairing instability mode arising in a row of identical two-dimensional vortices as sketched in figure 6-c.
The growth rate σ of the most unstable mode is presented as a function of L for core size $a = 0.09$ on figure 7-a: the growth rate decreases as L increases. Because of the numerical accuracy limitation mentioned above, the spectrum contains always a positive growth rate. However, there exist a value of L for which the numerically estimated

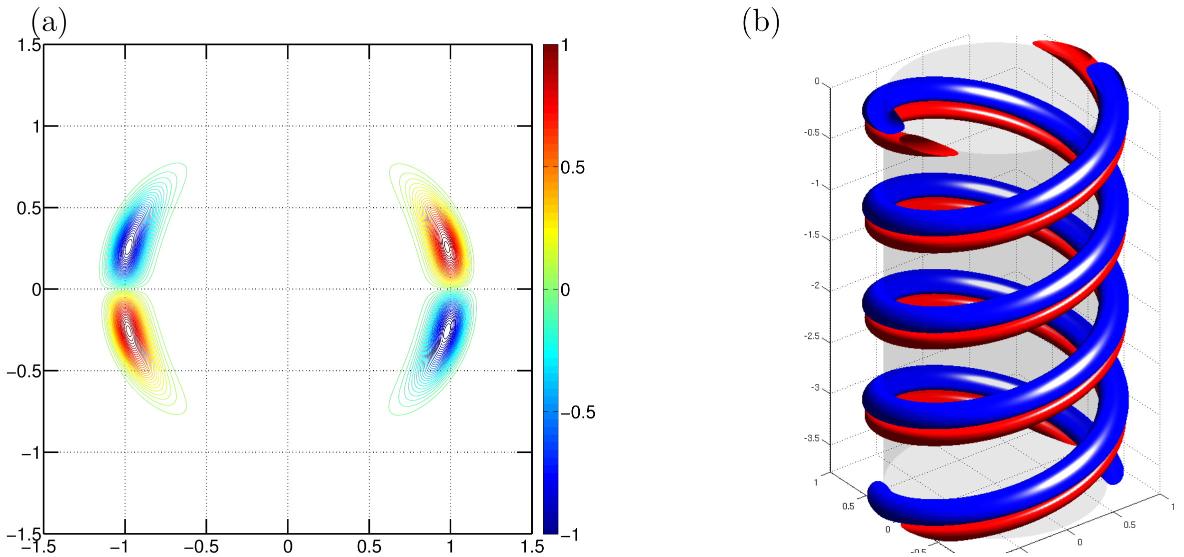

Figure 5: Neutral mode for two helical vortices at $L = 0.3, a = 0.09$ and $Re = 10000$ (red circle in figure 4). (a) Contours of the real part of $\hat{\omega}_B$ in the plane orthogonal to the $z-$axis. (b) Three-dimensional iso-surface of vorticity corresponding to $\pm \max \Re\{\hat{\omega}_B\}/4$ (red for positive and blue for negative values).

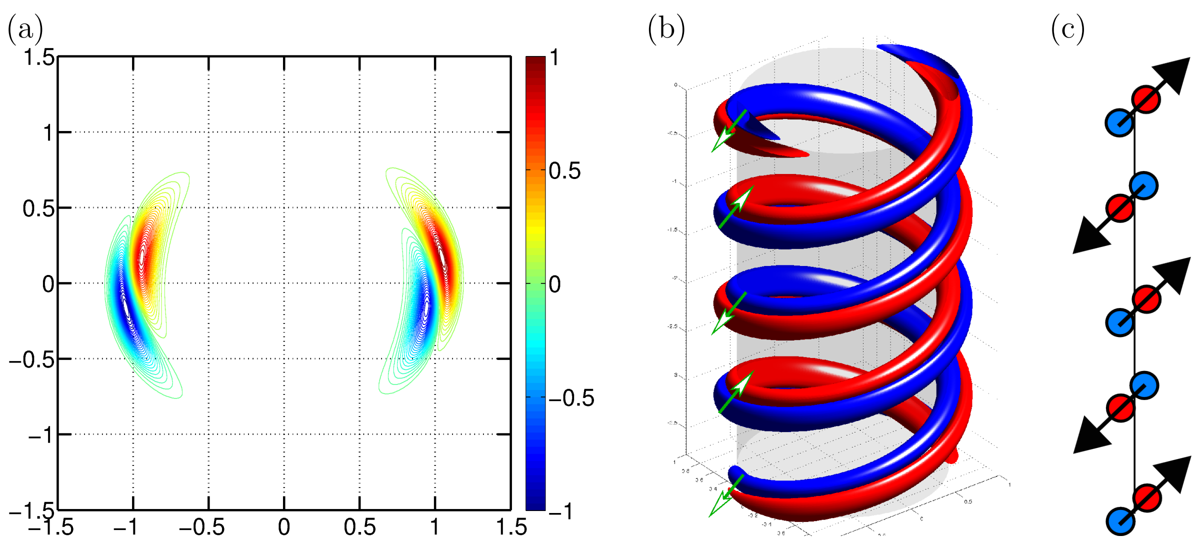

Figure 6: The most unstable mode for two helical vortices at $L = 0.3$, $a = 0.09$ and $Re = 10000$. (a) Contours of the real part of $\hat{\omega}_B$ in the plane orthogonal to the $z-$axis. (b) Three-dimensional iso-surface of vorticity corresponding to $\pm \max \Re\{\hat{\omega}_B\}/4$ (red for positive and blue for negative values). Arrows indicate the displacement induced by the mode: one vortex goes inwards while the other goes outwards. (c) Schematic representation in the meridional (r, z) plane: the structure is analogous to a pairing instability mode for an infinite row of point vortices.

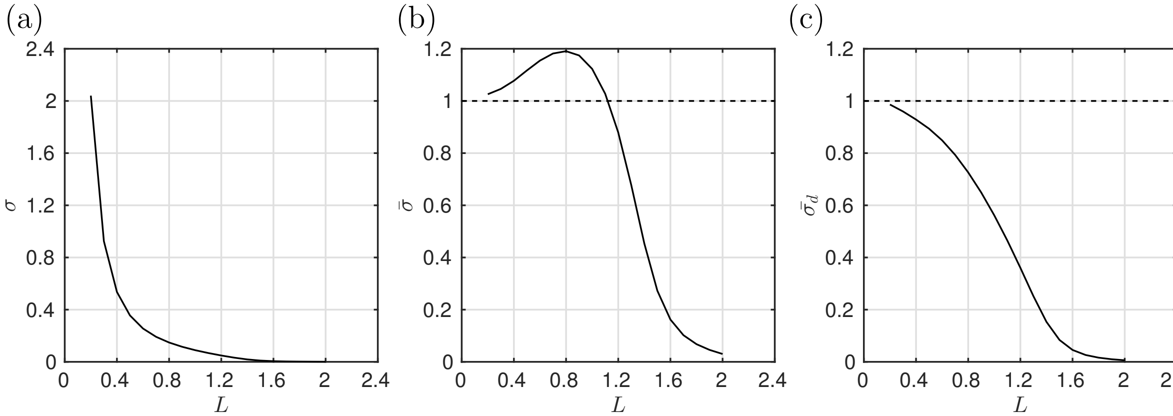

Figure 7: Most unstable instability mode for two helical vortices with $a = 0.09$, $Re = 10000$. (a) Maximum growth rate $\sigma(L)$. (b) Normalized growth rate $\bar{\sigma}(L)$ (see equation (25)). (c) Normalized growth rate $\bar{\sigma_d}(L)$ (see equation (27)).

maximum growth rate equals the value obtained for the neutral mode. This value $L \sim 1.6$ can be considered as the stability threshold. In the inviscid framework, Okulov & Sørensen [11] predicted that two helical Rankine vortices are unstable for $L < 1.106$. For the present configuration, a higher threshold is found. This difference could be attributed to the nature of the underlying vorticity profile (it is nearly Gaussian) and to the finite Reynolds number effect.

4.1. Point vortex and vortex ring analogies for two helical vortices

In this section, we go back to dimensional quantities for the sake of clarity. When visualised in the meridional plane (figure 6-c), the instability mode looks very similar to the unstable mode of an infinite row of point vortices separated by an axial distance $h = 2\pi L/N$ with $N = 2$, i.e. from the distance between two successive patterns in figure 6-c. More quantitatively, we compare following [15], the growth rates computed for helical configurations to the values for an infinite array of two-dimensional point vortices. The maximum growth rate of such an array [24, 25] is equal to $\sigma_{2D}(h_p) = \Gamma\pi/4h_p^2$ where Γ and h_p respectively stand for the circulation and separation of point vortices. One may tentatively compare growth rates obtained for helical vortices to those obtained for point vortices separated by a distance $h_p = h$:

$$\bar{\sigma}(L) \equiv \frac{\sigma(L)}{\sigma_{2D}(h)} = 16\frac{\pi L^2 \sigma(L)}{\Gamma N^2}, \tag{25}$$

Figure 7-b depicts the normalised growth rate $\bar{\sigma}(L)$ for core size $a/R = 0.09$ as a function of L. For small values of L, it tends towards unity indicating that the instability mechanism is similar to the pairing of point vortices. For increasing L, $\bar{\sigma}$ exceeds one, which would imply an enhancement of instability compared to the point vortex array instability. However, this is rather due to the choice of h as the separating length h_p between point vortices. Indeed, following Quaranta *et al.* [17], unwrapping the successive

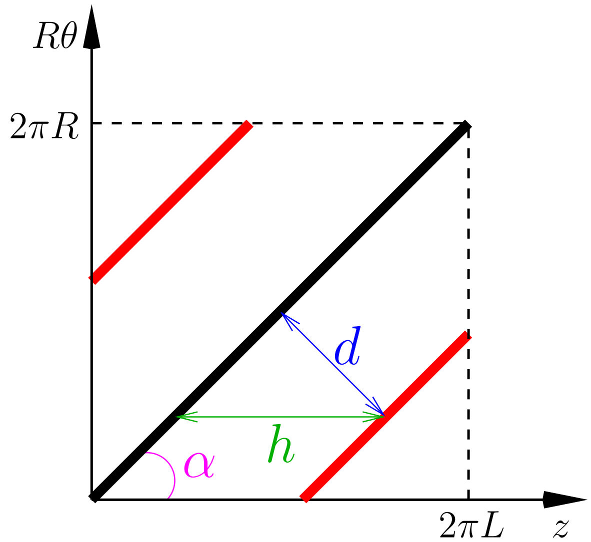

Figure 8: Schematic representation of the shortest length d between two successive coils for two helical vortices.

coils in a $(z, R\theta)$-plane as depicted in figure 8 reveals the shortest length between two successive coils to be

$$d = h \sin\alpha = \frac{2\pi L}{N} \frac{R}{(L^2 + R^2)^{1/2}} \tag{26}$$

rather than h. Using $h_p = d$ instead of $h_p = h$ leads to a different normalized growth rate

$$\bar{\sigma_d}(L) = \frac{\sigma(L)}{\sigma_{2D}(d)} = \bar{\sigma}(L) \frac{R^2}{L^2 + R^2} \tag{27}$$

plotted in figure 7-c for $a/R = 0.09$. In that case, growth rate $\bar{\sigma_d}(L)$ monotonically decreases when L increases tending to one as L goes to zero. This indicates no peculiar instability enhancement. In addition, stabilisation is expected as L increases since the system tends towards two point vortices.

Growth rates may also be compared to those obtained in the case of an infinite array of vortex rings of circulation Γ, radius R separated by an axial distance h. Using a filament approach [26], the maximum growth rate σ_{Ring} of the pairing instability for uniform vorticity ring arrays, was found to be

$$\sigma_{Ring} = \frac{\Gamma}{2\pi R^2} \sqrt{C\left(G + C/2 - B + H_0\right)} \tag{28}$$

with

$$B = \sum_{p=1}^{\infty} \frac{\alpha_{2p-1}^3}{2} \left[\left(3 + \beta_{2p-1}^2\right) E\left(\alpha_{2p-1}^2\right) - K\left(\alpha_{2p-1}^2\right)\right], \tag{29}$$

$$C = \sum_{p=1}^{\infty} \alpha_{2p-1}^3 \left[\left(1 - \beta_{2p-1}^2\right) E\left(\alpha_{2p-1}^2\right) - K\left(\alpha_{2p-1}^2\right)\right], \tag{30}$$

$$G = \sum_{p=1}^{\infty} \alpha_{2p}^3 \left[2E\left(\alpha_{2p}^2\right) - K\left(\alpha_{2p}^2\right) \right], \tag{31}$$

$$\alpha_k = \left[1 + \left(\frac{kh}{2R} \right)^2 \right]^{-1/2}, \quad \beta_k = \frac{2R}{kh}. \tag{32}$$

The functions K and E are the complete elliptic integrals of the first and second kind, respectively [27]. The last term

$$H_0 = \frac{1}{2}\left(\frac{7}{4} - \ln \frac{8R}{a_e} \right) \tag{33}$$

is associated to the self-induced velocity of a single ring with uniform vorticity i.e. a Rankine profile of core size a_e. The above formulae were extended by [16] for vortex rings with arbitrary vorticity profiles. Indeed it is known [28] that equation (33) can be used for arbitrary vorticity profiles if one defines an equivalent core size a_e. The vorticity profile in such helical vortices is close to a Gaussian [20] of size a: the equivalent core size is then $a_e \approx 1.36a$ [16].

Going back from now on to dimensionless quantities, growth rates σ can be directly compared to those obtained for vortex rings separated by a distance $h = 2\pi L/N$ (see figure 9-a) or indirectly by plotting the normalized growth rate $\sigma/\sigma_{ring}(d)$ (see figures 9-b). For pitch values $L < 0.4$, growth rates obtained for vortex rings and two helical vortices are very similar. A deviation is observed for $L > 0.4$. For larger L, whatever the core size a investigated, the growth rate monotonically decreases.

4.2. Influence of the core size a and Reynolds number

The influence of the core size on the growth rate is found weak for the range of a investigated ($0.06 \leq a \leq 0.1$) (see figure 9). For fixed value of $L > 0.4$, the growth rate increases when the core size is decreased. As shown by Brancher & Chomaz [29], vorticity concentration enhances the pairing instability even though this effect is relatively weak. The limit $L = 0$ cannot be reached since the finite core size implies $L \gtrsim Na$. For $N = 2$, $a = 0.09$, this imposes $L \gtrsim 0.18$.

The influence of the Reynolds number on the growth rate $\bar{\sigma}$ has been investigated for core sizes $a = 0.06$ and $a = 0.09$ (figure 10). It is observed that the Reynolds number has a weak effect and that the growth rate seems to be slightly enhanced at low values of the Reynolds number. There is no clear mechanism to account for this unexpected behaviour which has been checked to be numerically robust.

4.3. Influence of a central hub vortex

We investigate the influence of a central hub of dimensionless circulation -2 on the stability of two helical vortices. In our simulations, the hub core size is chosen equal to the core size a of the helical vortices. The most unstable mode is depicted for $L = 0.3$, $a = 0.09$ and $Re = 10000$ on figure 11. The mode structure for the helical vortices is

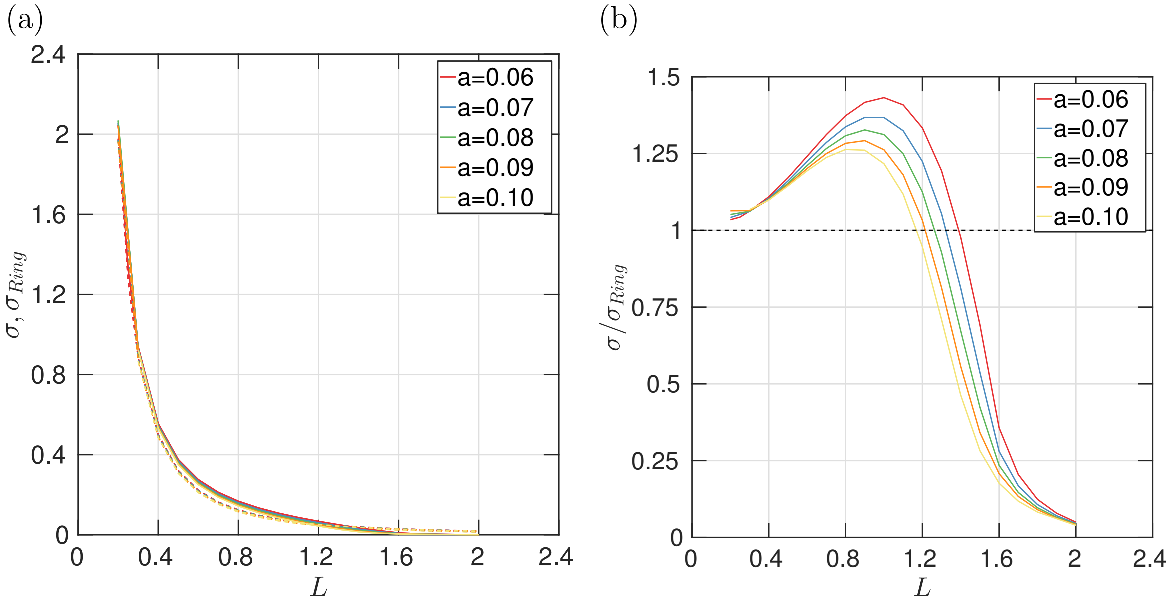

Figure 9: Most unstable mode for two helical vortices for $a = 0.06, 0.07, ..., 0.1$ at $Re = 10000$. (a) Maximum growth rate $\sigma(L)$ (solid line) and $\sigma_{Ring}(d)$ (dashed lines) as a function of L. (b) Normalized growth rate $\sigma(L)/\sigma_{Ring}(d)$ as a function of L.

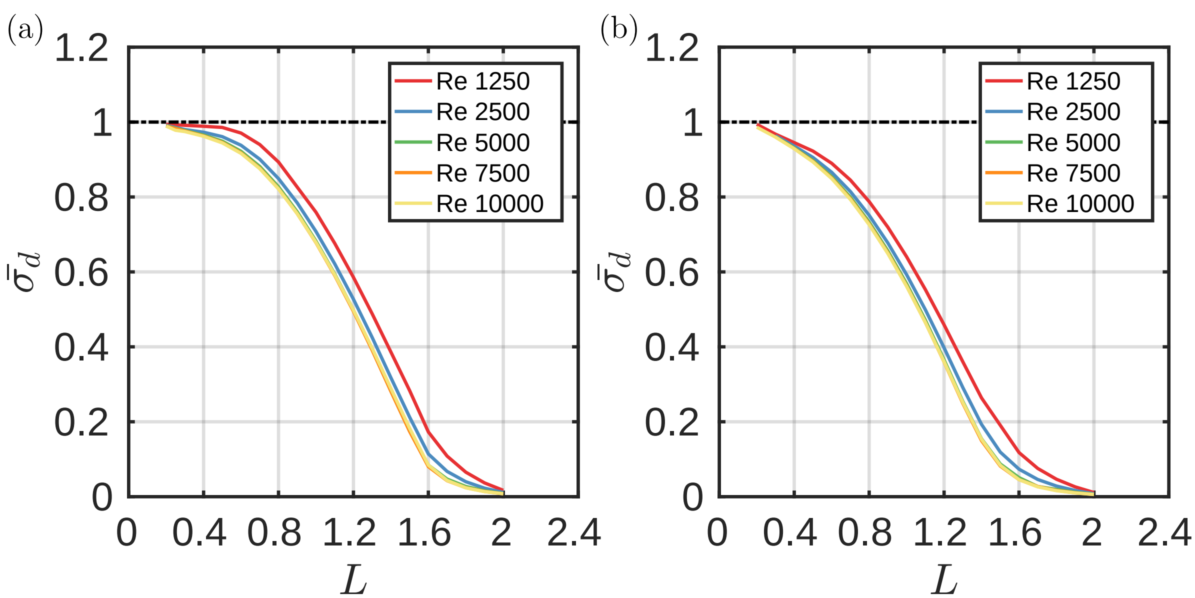

Figure 10: Influence of the Reynolds number on the normalized growth rate $\bar{\sigma}(L)$ for two helical vortices. (a) core size $a = 0.06$; (b) core size $a = 0.09$.

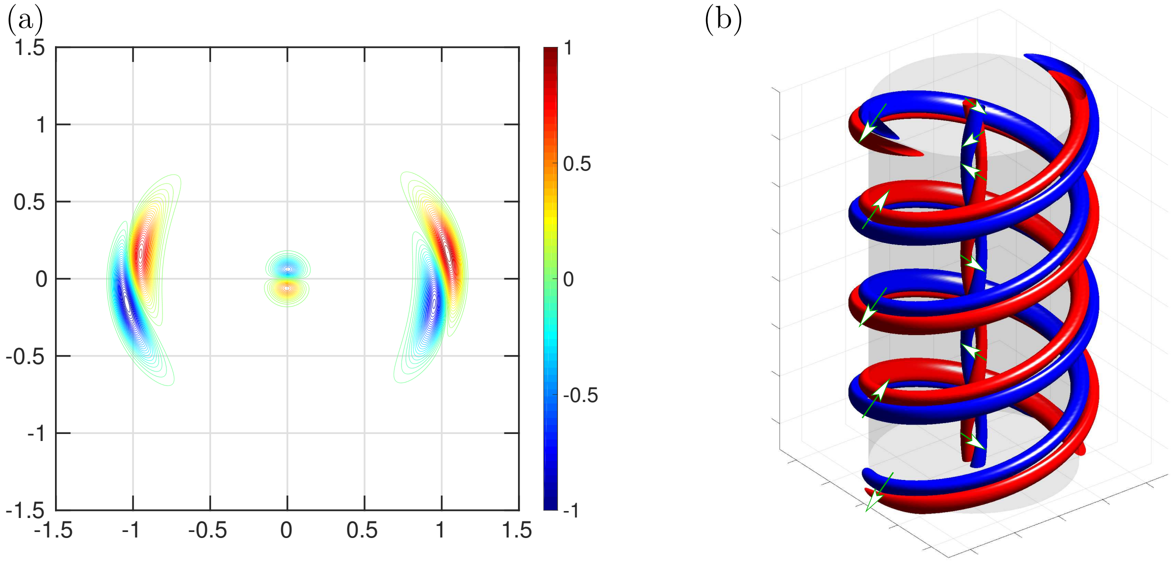

Figure 11: Most unstable mode for $Re = 10000$ with the base flow composed of two helical vortices with $L = 0.3$, core size $a = 0.09$ and a central hub vortex with identical core size. (a) Contours in the plane orthogonal to the $z-$axis of $\Re\{\hat{\omega}_B\}$. (b) Schematic representation showing the displacements (represented with green arrows) induced by the unstable mode.

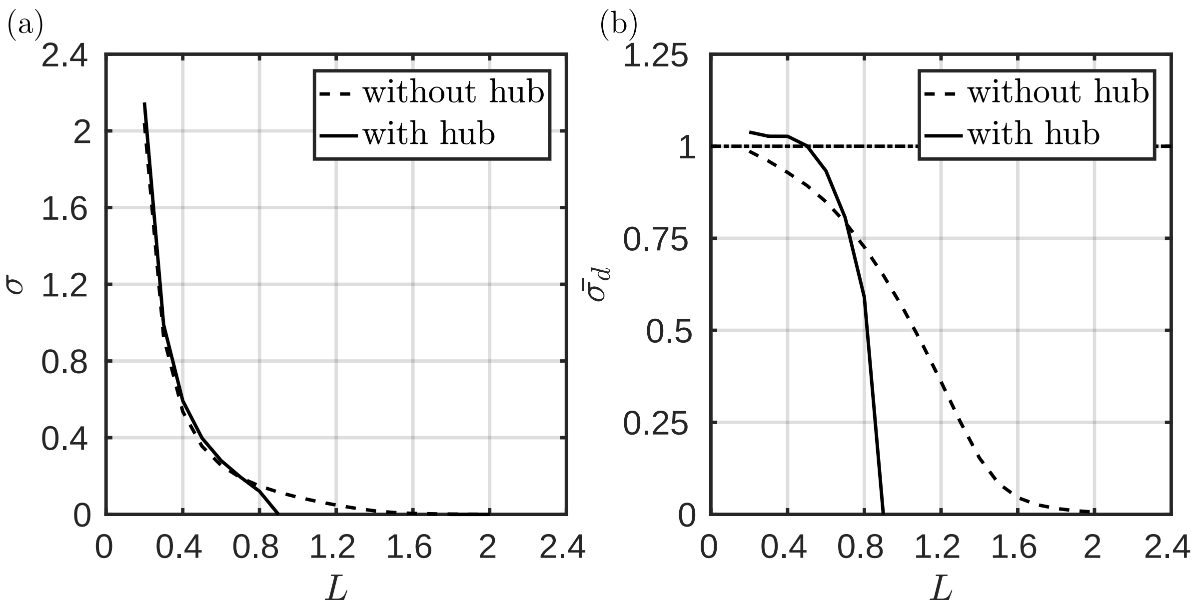

Figure 12: Dominant instability mode for two helical vortices with the vortex hub (solid line) and without (dashed line) for $a = 0.09$ and $Re = 10000$. (a) Growth rate $\sigma(L)$ as a function of pitch L. (b) Normalized growth rate $\bar{\sigma_d}(L)$.

similar to the case without hub: it induces a displacement of these helical vortices. In addition, the hub vortex is displaced in the same "direction". Such phenomenon was experimentally observed [14] in a water channel downstream of propellers. The growth rate is plotted in figure 12 as a function of L. For $L < 0.7$, the difference between growth rates with and without hub is always of the same positive sign though it is of order of the numerical precision: one may thus conclude that the instability is unchanged or only slightly enhanced by the presence of a central hub. On the contrary, for $L > 0.7$, the growth rate abruptly decreases when the hub is present and the system stabilises near $L = 0.9$.

5. Nonlinear evolution of two helical vortices in the helical framework

For small pitches, helical vortices are similar to vortex ring arrays, for large pitches to straight vortices. Consequently, helical vortices might be subjected to mechanisms observed in vortex rings and straight vortices. More precisely, one observes the well-known leapfrog mechanism [24, 25] for several vortex rings and merging occurs for several straight vortices when they are sufficiently close to each other [30, 31]. In this section, we analyse the nonlinear evolution of helical arrays when they are perturbed by the unstable mode obtained in section 4, their dynamic being restricted to helical symmetry. Numerical computations which are performed using the HELIX code, are thus initiated with

$$\omega_B^{\mathrm{Total}} = \omega_B^{\mathrm{BF}} + A\Re\{\hat{\omega}_B\}, \quad u_B^{\mathrm{Total}} = u_B^{\mathrm{BF}} + A\Re\{\hat{u}_B\}, \tag{34}$$

where u^{BF}, ω^{BF} are the basic flow components (see for instance figure 2-a for ω_B^{BF}) and $\hat{\omega}_B$, $\hat{u}_B$ are the instability mode components (see for instance figure 6-a for $\hat{\omega}_B$). This disturbance generates a small asymmetry between the two vortices by radially shifting one of them. In the experiment by Bolnot [15], a somewhat similar asymmetry was generated between the two blades of a rotor by radially shifting one of them. Finally, amplitude A is set to $A = 0.01 \left\|\boldsymbol{\omega}^{\mathbf{BF}}\right\|$ with $\|.\|$ being the Euclidean norm. Such a value guarantees the initial stage of the evolution to remain in the linear regime. The nonlinear regime is then characterised by tracking the radial position $r_A(t)$ of each vortex centreline. More precisely, the maximum of the helical vorticity component for each vortex is radially located at $r_A(t)$.

5.1. Leapfrog or overtaking of two helical vortices

The nonlinear saturation dynamics of two helical vortices can be described as follows: the radius of one vortex decreases while the radius of the other one increases leading to the acceleration of the smaller one passing through the larger one. Snapshots of this basic sequence at $Re = 10000$ of two vortices of pitch $L = 0.30$ with initial core size $a = 0.06$ are shown in figure 13. This basic sequence repeats itself, but this can occur in two different ways, denoted as *leapfrogging* and *overtaking*. In the *leapfrog* dynamic, vortices exchange their roles between two successive sequences. This mechanism was evidenced for spatially evolving helical vortices [15, 32, 33]. It is observed here numerically in the framework of helical symmetry (light grey areas in figure 14). In the *overtaking* dynamic, the overtaking vortex is the same for two successive sequences. This new behaviour has been found for intermediate values of $L \geq 0.5$ at $a = 0.06$ (light green

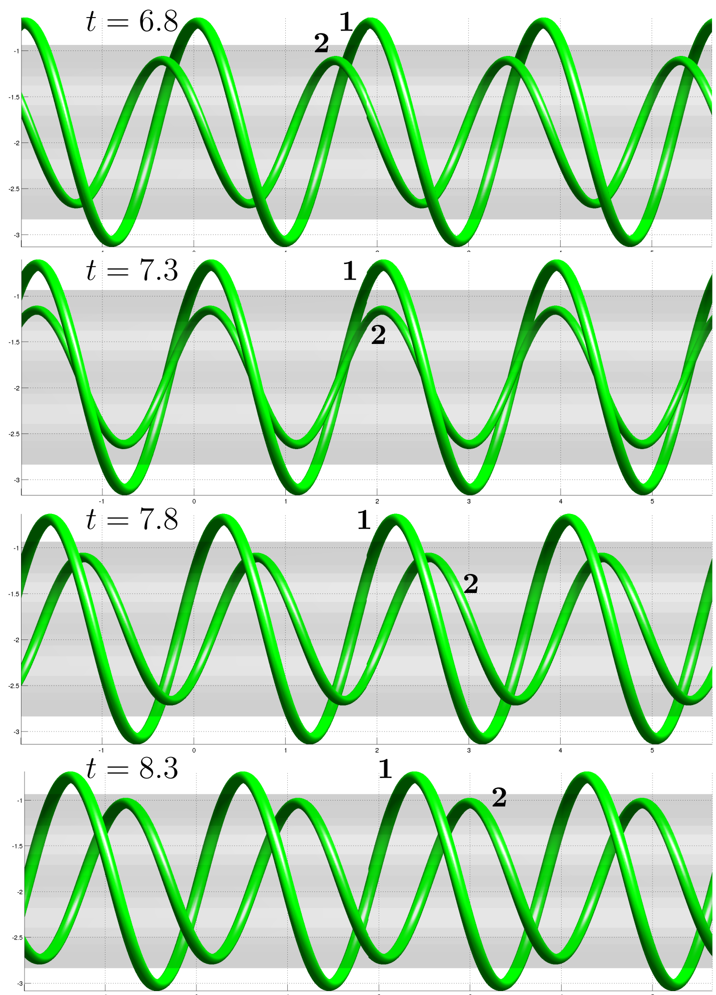

Figure 13: Basic sequence of the nonlinear evolution of two helical vortices perturbed with the unstable mode. Case $L = 0.3$, initial core size $a = 0.06$ and $Re = 10^4$. Iso-surface of the helical vorticity $\omega_B = \frac{1}{4}\omega_B^{max}(t)$. The grey region is the cylinder of radius $R = 1$. Vortices are labelled (1 and 2) so that they can be tracked in time.

areas in figure 14) and also at lower pitch for smaller initial core sizes $a = 0.03$. During overtaking sequences, the helix radius of one vortex remains greater than one, and greater than the radius of the companion vortex. The overtaking dynamic when present is always followed by leapfrogging. As a consequence, we define the *time of first leapfrog* as the time when the two vortex radii are identical. When no overtaking is present, this corresponds to the first crossing after the initial condition (see figure 14-b). When overtaking sequences are present, the *time of last overtaking* is defined as the beginning of the basic sequence preceding the time of first leapfrog (see figure 14-c). Because of viscous diffusion, the basic sequence illustrated in figure 13 ceases to be observed after a certain time. This is associated to the onset of merging as will be shown in §5.2. The *onset of merging time* corresponds to the final time of the last observable basic sequence (see figure 14-b).

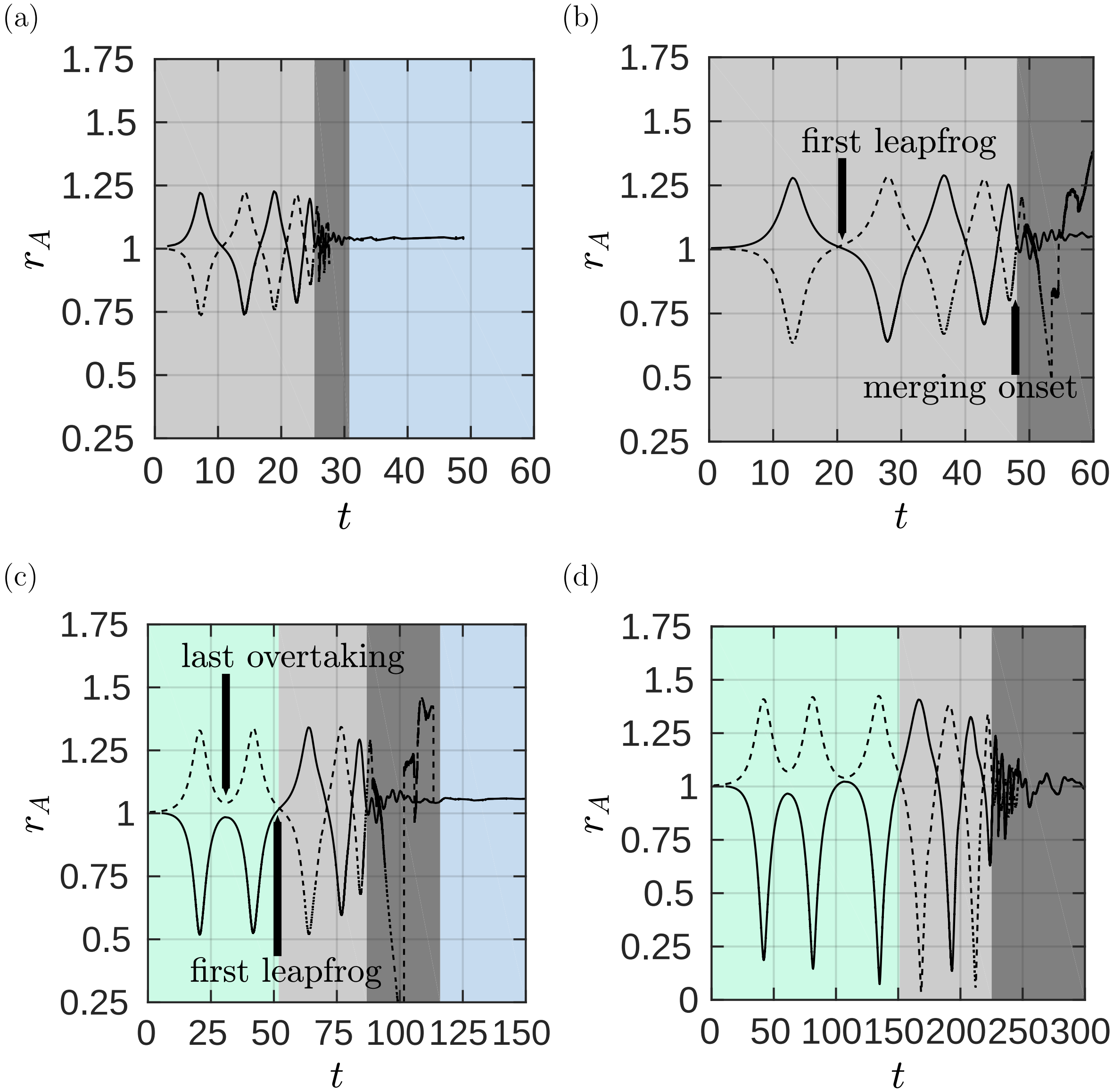

Figure 14: Influence of the reduced pitch L on the time evolution of vortex centres r_A at $Re = 10000$ and initial core size $a = 0.06$, for (a) $L = 0.3$, (b) $L = 0.4$, (c) $L = 0.5$ and (d) $L = 0.7$. The light green region corresponds to the overtaking phase, the light grey area to the leapfrog phase, the dark grey area to the merging period and the blue region to the merged state.

5.1.1. Influence of the reduced pitch L Let us perturb the two helical vortices of initial fixed core size $a = 0.06$ for Reynolds number $Re = 10000$. The radial position $r_A(t)$ are plotted with respect to time in figure 14 for various values of $0.3 \leq L \leq 0.7$. Cases $L = 0.3$ (figure 14-a) and $L = 0.4$ (figure 14-b) have similar dynamic i.e. vortices undergo several leapfrog events and then merge: 5 leapfrog events (light grey area) are observed before merging starts (dark grey area). For $L \geq 0.5$, vortices first undergo several overtaking events (figure 14-c and d). The number of overtaking events increases with

L	0.3	0.4	0.5	0.6	0.7	0.8
number of overtakings	0	0	2	3	3	3
number of leapfrogs	5	5	3	3	4	5
time of the last overtaking			30.53	75	107.5	142.6
a^{th}/h at the last overtaking			0.08	0.0972	0.0982	0.1013
time of the first leapfrog	10.65	20.24	51.9	105.1	151.1	200
a^{th}/h at the first leapfrog	0.941	0.1081	0.0994	0.1133	0.1151	0.1148
time of merging onset	25.25	48.25	86.8	152.9	221	346
a^{th}/h at merging onset	0.1242	0.1204	0.1247	0.1350	0.1379	0.1499

Table 1: Influence of pitch L on the nonlinear dynamics of two helical vortices with initial core size $a = 0.06$ at $Re = 10000$.

a_0	0.03	0.06	0.80	0.10
number of overtakings	2	0	0	0
number of leapfrogs	4	5	4	3
a^{th}/h at the first leapfrog	0.1008			
a^{th}/h at merging onset	0.1229	0.1248	0.1242	0.1284

Table 2: Influence of the initial core size a on the nonlinear dynamics of two helical vortices at pitch $L = 0.3$ and Reynolds number $Re = 10000$.

L while they occur at a slower pace (see table 1 which also contains values for $L = 0.6$ and $L = 0.8$). In addition, the peak amplitude increases with L so that for $L \geq 0.7$, the inner vortex gets near the $z-$axis (figure 14-d). After a few overtaking events, the vortices start leapfrogging. From the same figures, it can be seen that the number of leapfrogs also increases with L and that the events occur again at a reduced pace. Table 1 provides some additional informations: the values of a^{th}/h evaluated at the time of the last overtaking event and of the first leapfrog, with $a^{th}(t) = \sqrt{a_0^2 + 4t/Re}$. There exists a critical ratio $a^{th}/h \approx 0.10$ which separates the overtaking regime from the leapfrog regime.

5.1.2. Influence of the core size a The influence of the initial core size on the nonlinear evolution is analysed by varying the initial core size from 0.03 to 0.1 while keeping constant the Reynolds number at $Re = 10000$ and the reduced pitch at $L = 0.3$. Figure 15 displays the time evolution of the radial position of the vortex centres. Overtaking is only observed for the smallest core size considered ($a = 0.03$) and table 2 shows that the value $a^{th}/h = 0.10$ is compatible with the threshold found previously. For larger core sizes, only leapfrog is observed and as the initial core size increases the number of leapfrogs reduces (see table 2). This can be explained by looking at the values of critical a^{th}/h measured at the onset of merging. Table 2 indicates a constant critical ratio of 0.12: this ratio is reached in a shorter time as the initial core size is increased, so that

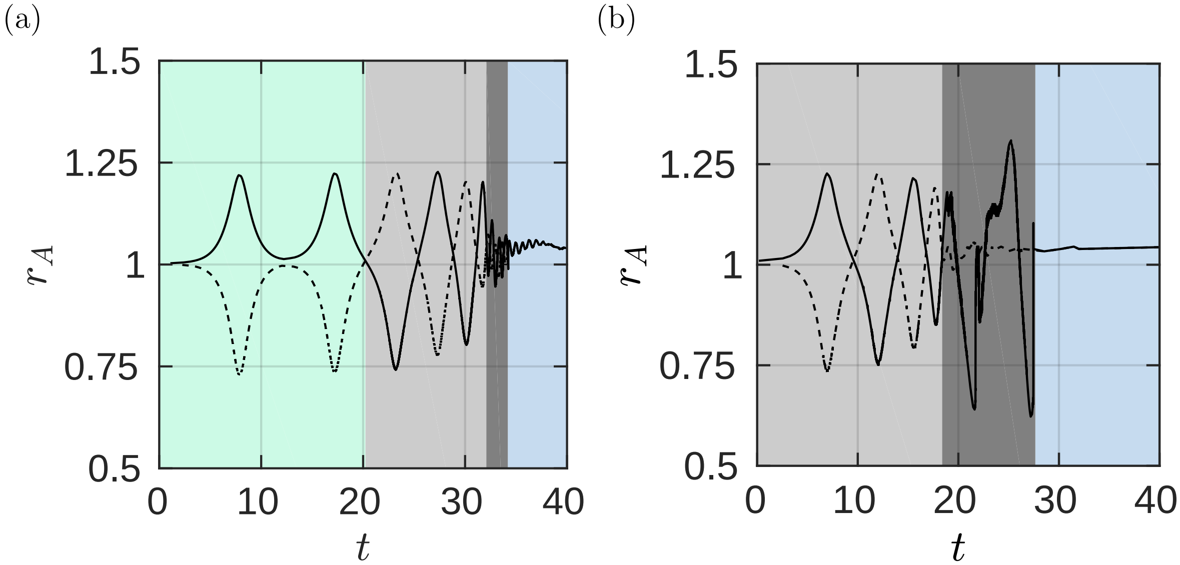

Figure 15: Influence of the initial core size on the dynamic of two helical vortices of pitch $L = 0.3$ at $Re = 10000$. Simulations are initialised with core sizes (a) $a = 0.03$ and (b) $a = 0.08$. The evolution of r_A as a function of time is displayed: the solid line tracks one vortex and the dashed line its companion. The light green region corresponds to the overtaking phase, the light grey area to the leapfrog phase, the dark grey area to the merging period and the blue region to the merged state.

Re	1250	2500	3750	5000	6750	10000
number of leapfrogs	1	2	3	4	4	5
a^{th}/h at merging	0.1814	0.1515	0.1383	0.1369	0.136	0.1248

Table 3: Influence of the Reynolds number Re on the nonlinear dynamics of two helical vortices at pitch $L = 0.3$ with initial core size $a = 0.06$.

less leapfrog events occur. The amplitude of the initial leapfrog seems independent of the initial core size a.

5.1.3. Influence of the Reynolds number Re The influence of the Reynolds number is investigated here for constant pitch value $L = 0.3$ at fixed initial core size $a = 0.06$. The number of leapfrogs increases with the Reynolds number (see figure 16 and table 3). This observation is compatible with the existence of a critical ratio a^{th}/h for the onset of merging found here to be approximately $a^{th}/h \approx 0.13$: this ratio is reached later in time for higher Reynolds numbers.

5.2. Merging of two helical vortices

The merging of large pitch helical vortices ($L \geq 1$) has already been investigated numerically for two [34] and three vortices [35]. It can be related to the merging of

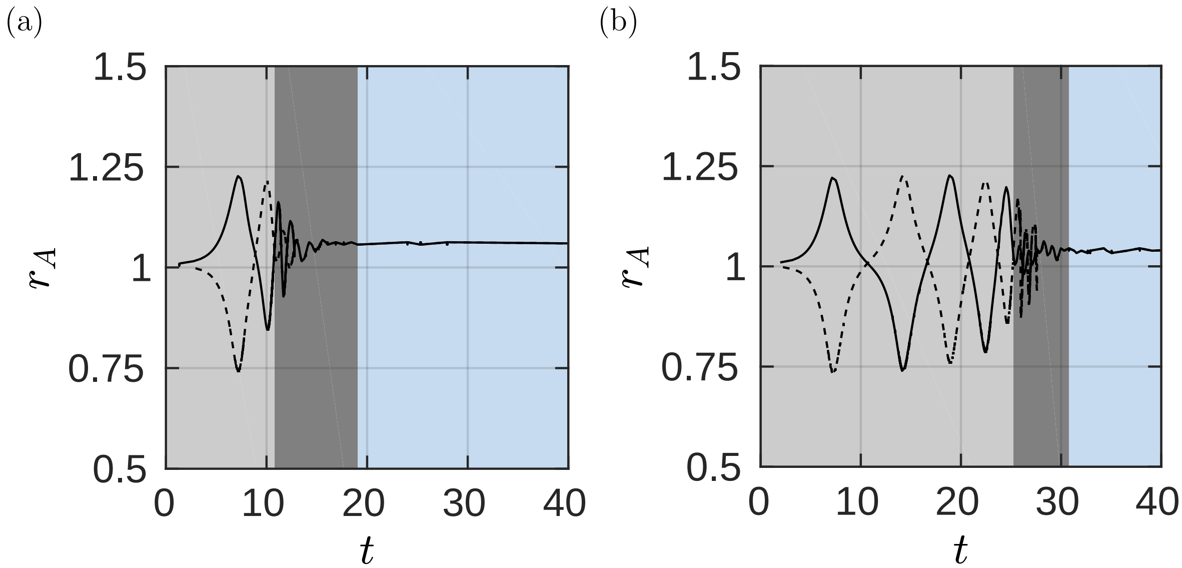

Figure 16: Influence of the Reynolds number on the leapfrog mechanism for two helical vortices of pitch $L = 0.3$ and core size $a = 0.06$ at (a) $Re = 2500$ and (b) $Re = 10000$. The evolution of r_A is shown as a function of time. The grey region indicates the time interval when leapfrogs occur, the dark grey represents the merging phase and the light blue region indicates the merged state.

straight vortices. At lower L values, the situation is different and involves successive coils. Merging thus occurs after leapfrog events: the process is illustrated in figure 17 at several instants. The view in the meridional plane (right column) shows the similarity of this process with merging in two-dimensional vortex arrays. Here, onset of merging of two vortices seems to be associated to a critical ratio $a^{th}/h \approx 0.13$.

6. Dynamics of three helical vortices in the helical framework

6.1. Linear stability results for three helical vortices

The three helical vortex system has two complex conjugate unstable modes. Figure 18 displays the structure of the unstable mode with positive ω for $L = 0.30$, $a = 0.09$ in the presence of a hub vortex. The perturbation is not zero at the hub location showing that the hub vortex is involved in the unstable dynamic. Growth rates are plotted in figure 19 as a function of L. The presence of a hub vortex destabilises the system. It increases growth rates and the critical pitch: the system stabilises as soon as $L > 1.6$ (resp. $L > 1.35$) with (resp. without) a hub. This effect is the opposite to what was observed for two vortices.

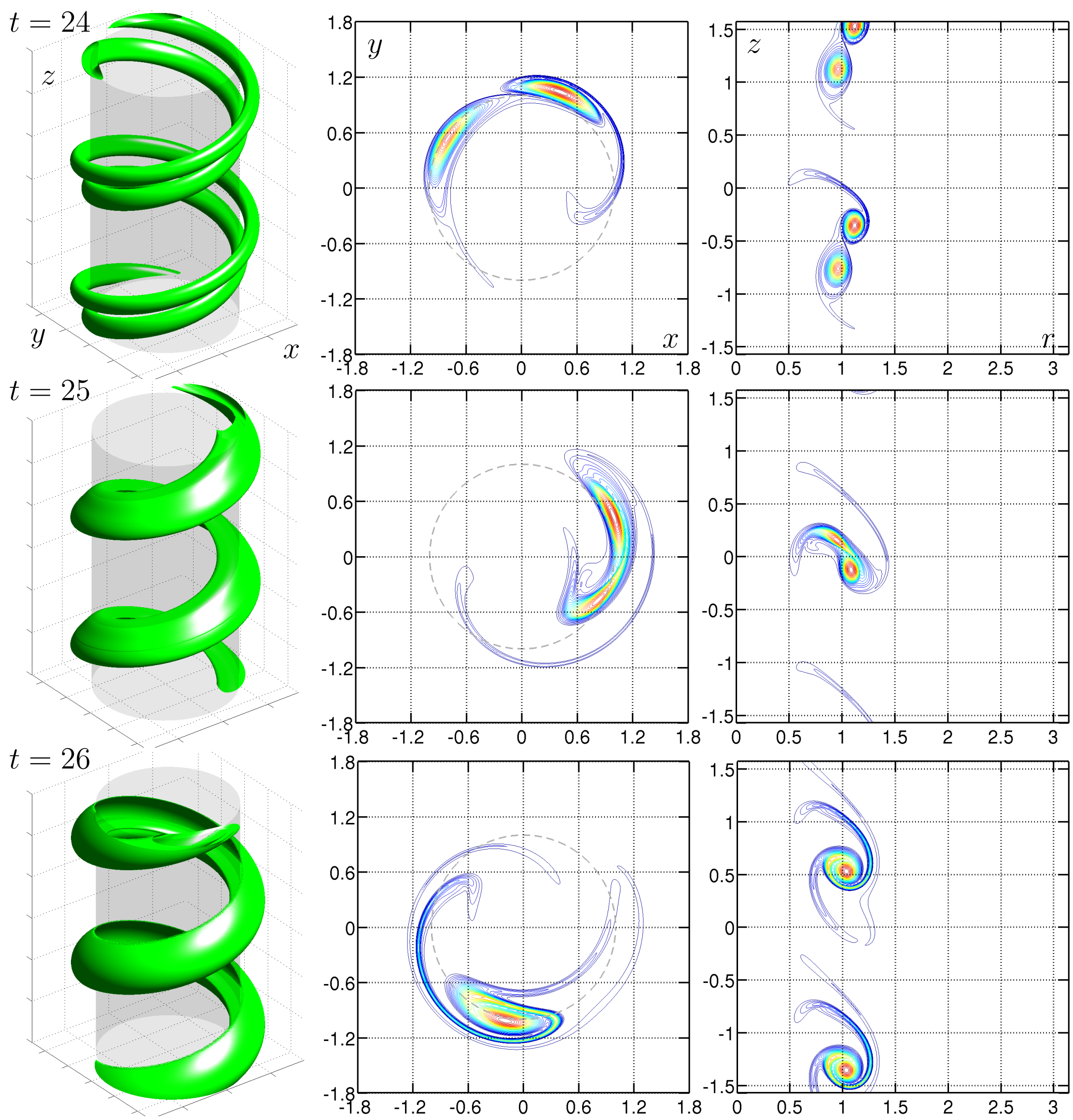

Figure 17: Merging at $Re = 10000$ of two helical vortices of pitch $L = 0.3$ and core size $a = 0.06$ perturbed initially with the helical pairing mode. Left: isovalue of the vorticity component $\omega_B = \frac{1}{4}\omega_B^{max}(t)$. Centre: contours of ω_B in the $z = 0$ plane. Right: contours of ω_B in the meridional $r - z$ plane.

6.2. Nonlinear evolution of three helical vortices

When initially perturbed by the unstable mode given in section 6.1, three helical vortices display complex dynamics involving successive leapfroggings, as can be seen for instance in figure 20 for $L = 0.3$ with a central hub vortex. The corresponding time evolution of the vortex radial positions r_A is plotted in figure 21-a. It reveals that a partial merging of two vortices first occurs at $t \approx 7$. The resulting vortex then leapfrogs with the last peripheral one before finally merging at $t \approx 10$. The central hub vortex is also affected

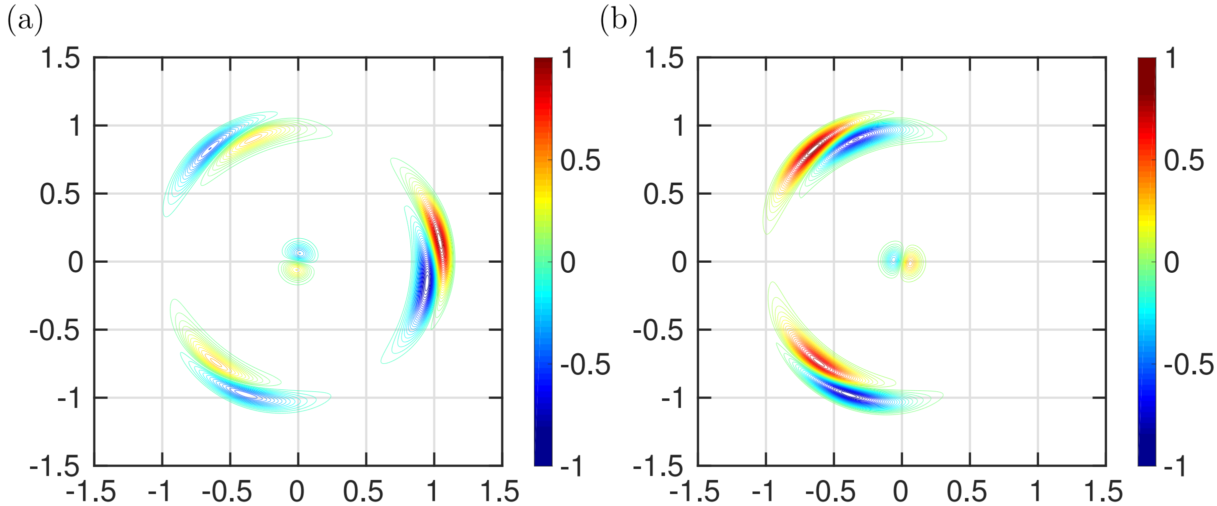

Figure 18: Structure of the instability mode with positive ω for three vortices with $L = 0.30$, $a = 0.09$ and a central hub. (a) Real part of the eigenvector $\hat{\omega}_B$. (b) Imaginary part of $\hat{\omega}_B$.

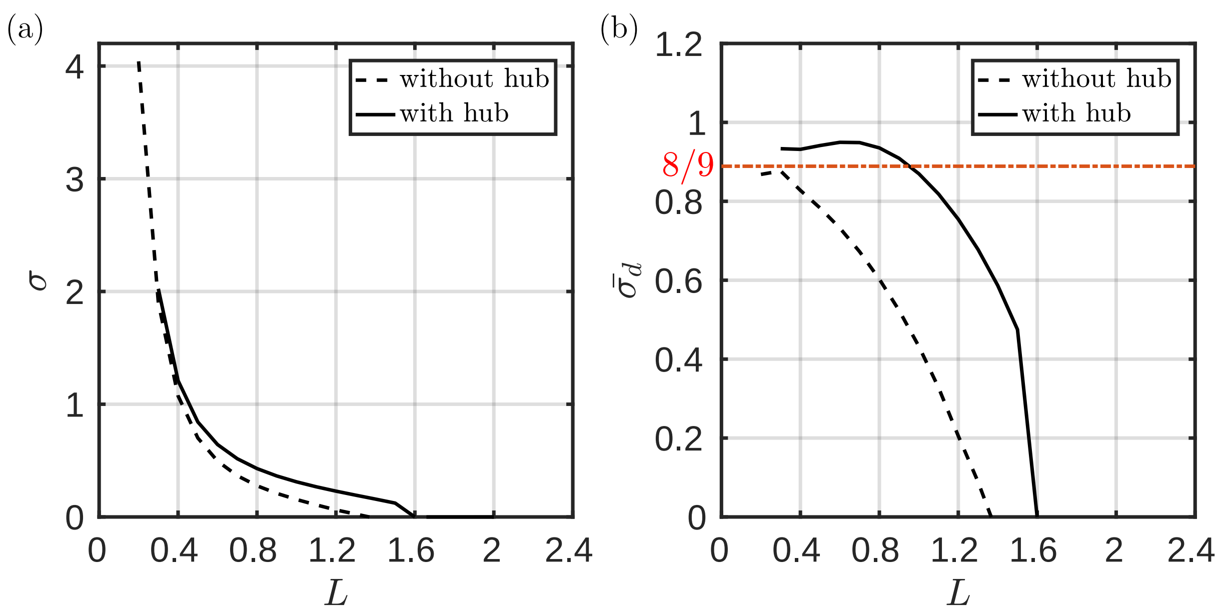

Figure 19: Dominant instability mode for $N = 3$ helical vortices with the vortex hub (solid line) and without (dashed line) with $a = 0.09$ at $Re = 10000$. (a) Growth rate $\sigma(L)$. (b) Normalized growth rate $\bar{\sigma}_d(L)$. It can be shown that the value of 8/9 displayed in graph (b) is the maximum growth rate achievable in the point vortex analogy of three helical vortices.

and oscillates in the vicinity of the $z-$axis. Peripheral vortices evolve in a similar way without hub vortex (figure 21-b), but the timescale is larger: the partial merging occurs at $t \approx 10$ and the final one at $t \approx 12.5$. At a larger pitch $L = 0.6$, vortices evolve on larger timescales when compared to similar cases at $L = 0.3$. However, the hub vortex acts in a similar way: systems evolve faster with hub vortex than without hub. As far as amplitudes are concerned, case $L = 0.6$ with hub reaches slightly higher amplitudes than $L = 0.3$, before the final merging occurs at $t \approx 32$ (see figure 21-c). The vortex system resulting from merging has a helical dipole structure, and the radii $r_A(t)$ for both opposite sign vortices show strong in-phase oscillations, with their amplitudes slowly increasing in time. For $L = 0.6$, amplitudes in presence of a hub vortex (figure 21-c) are much smaller than without (figure 21-d). The hub vortex thus limits the radial excursion of peripheral vortices. The merged state without hub (figure 21-d) also oscillates.

7. Concluding remarks

Using a dedicated DNS code, we obtained basic states defining various helical vortex configurations. An Arnoldi algorithm was then implemented on a linearised version of this code to determine the linear stability properties of such basic flow with respect to helically symmetric perturbations. For two or three helical vortex arrays, an unstable displacement mode was identified at low pitch. Its dependency with respect to pitch, core size, Reynolds number and presence of a hub vortex was also investigated. This mode was shown to be analogous to the pairing mode of an infinite array of point vortices or vortex rings. The nonlinear dynamics of two vortices perturbed by the displacement mode was thereafter computed in the framework of helical symmetry: a sequence of overtaking events, then leapfrogging and eventually merging were observed. Critical ratios a^{th}/h were determined for the transitions between these different sequences: $a^{th}/h \approx 0.10$ triggers the onset of leapfrogging and $a^{th}/h \approx 0.13$ triggers the merging. These values seem to be robust when varying the parameters (pitch, Reynolds, core size), but we cannot claim they are universal since we do not provide any physical explanation for them. Similar simulations were carried out for three helical vortices: the hub vortex enhances instability and globally accelerates the dynamic. However nonlinear oscillations of peripheral vortices may be limited when the hub is present.

This work was performed in parallel with laboratory experiments [15, 36] where typical values for the parameters were $Re = 10^4$, $L \approx 0.1$, $a = 0.05$, in the same range as our numerical study. Clearly, these Reynolds numbers are far below the values prevailing in wind turbine or helicopter applications, which are of order of $10^6 - 10^7$. The experimental measurements show the presence of different instabilities, in particular the one presented in this paper, that was named *global pairing* instability [36]: the experimental evaluation of the growth rate of this mode [15] coincides with the result obtained here at small L in figures 9 and 10. Values of L larger than 0.1 have not been investigated experimentally so far.

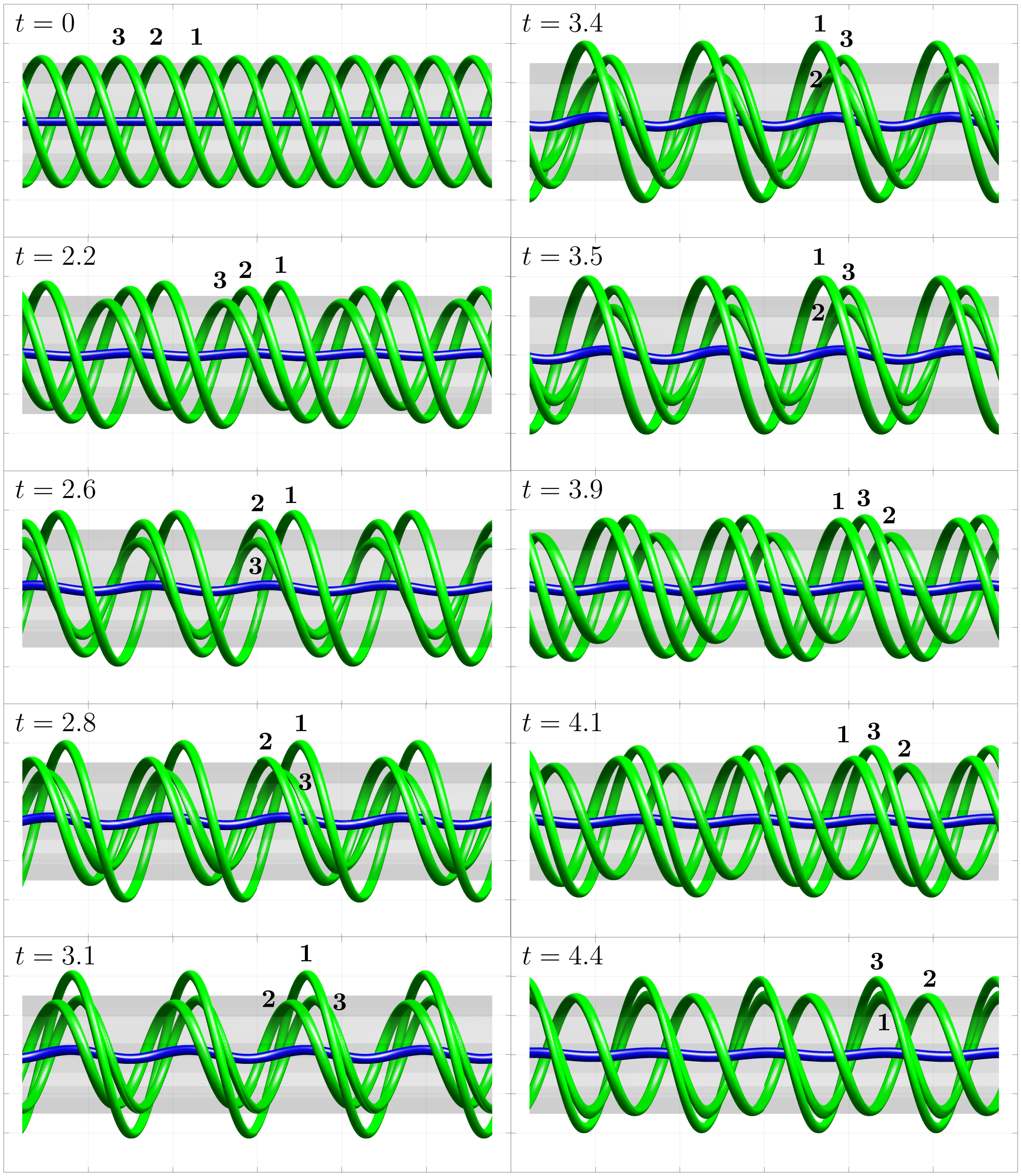

Figure 20: Temporal evolution of three vortices with a hub vortex initially perturbed by instability mode. Simulation at $Re = 10000$ with initial core size $a = 0.06$ and pitch $L = 0.3$. Isosurfaces of helical vorticity correspond to $\omega_B = \frac{1}{4}\omega_B^{max}(t)$. The grey region is the cylinder of radius $R = 1$. Vortices are labelled (1, 2 and 3) so that they can be tracked in time.

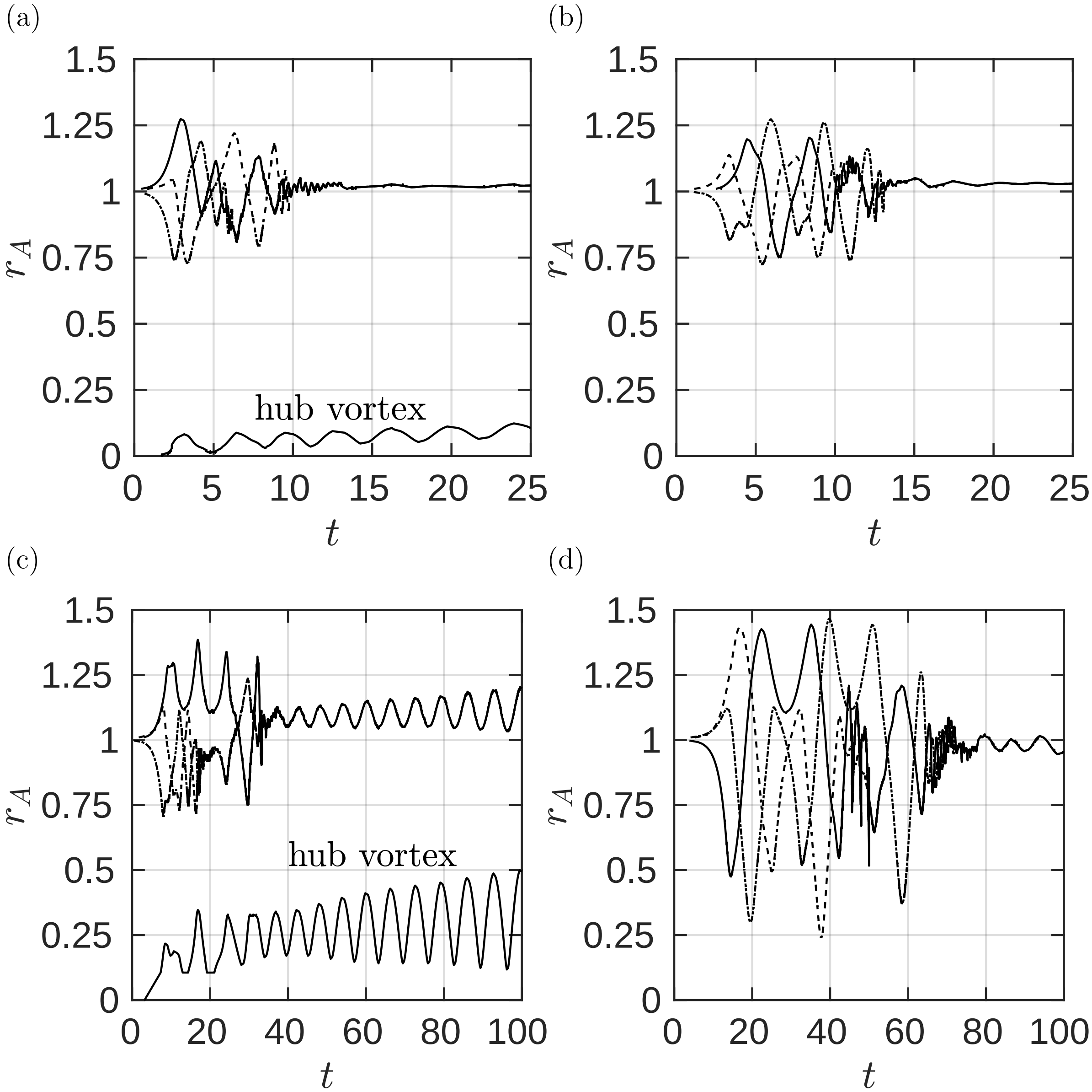

Figure 21: Temporal evolution of r_A for three vortices with a hub (figures a and c) or without (figures b and d). Simulations at $Re = 10000$ with initial core size $a = 0.06$ and pitch $L = 0.3$ (figures a and b) or $L = 0.6$ (figures c and d).

Regarding the nonlinear evolution of this global pairing mode, the basic sequence of figure 13 has been observed experimentally in a spatial setting. However the distinction between overtaking or leapfrogging is not accessible experimentally since only one basic sequence is observable in the existing facilities.

In experiments, many other modes exist although the global pairing mode dominates when present. These modes are *local pairing* modes that break the helical symmetry. They were thus excluded from the present analysis. An extension of the present linear instability study to modes breaking the helical symmetry has been performed numerically [19] and found able to reproduce the stability curves of local pairing modes.

These results are beyond the scope of the present paper.

Acknowledgments

This work received support from the French Agence Nationale de la Recherche under the ANR HELIX project ANR-12-BS09-0023-01. HPC resources from GENCI-IDRIS (grants 2015-2a1386 and 2016-2a1386) are also acknowledged, as well as technical help from Jalel Chergui.

References

[1] Hardin J C 1982 *Phys. Fluids* **25** 1949

[2] Dritschel D G 1991 *J. Fluid Mech.* **222** 525–541

[3] Ricca R L 1994 *Journal of Fluid Mechanics* **273** 241–259 ISSN 1469-7645 URL `http://journals.cambridge.org/article_S0022112094001928`

[4] Kuibin P A and Okulov V L 1998 *Phys. Fluids* **10** 607

[5] Wood D H and Boersma J 2001 *Journal of Fluid Mechanics* **447** 149–171 ISSN 0022-1120, 1469-7645 URL `http://www.journals.cambridge.org/abstract_S002211200100578X`

[6] Fukumoto Y and Okulov V L 2005 *Phys. Fluids* **17** 107101

[7] Lucas D and Dritschel D G 2009 *Journal of Fluid Mechanics* **634** 245–268 ISSN 1469-7645 URL `http://journals.cambridge.org/article_S0022112009007319`

[8] Widnall S E 1972 *J. Fluid Mech.* **54** 641–663 ISSN 1469-7645

[9] Gupta B and Loewy R 1974 *AIAA Journal* **12** 1381–1387 ISSN 0001-1452 URL `http://dx.doi.org/10.2514/3.49493`

[10] Okulov V L 2004 *J. Fluid Mech.* **521** 319–342

[11] Okulov V L and Sørensen J N 2007 *J. Fluid Mech.* **576** 1–25

[12] Hattori Y and Fukumoto Y 2009 *Physics of Fluids (1994-present)* **21** 014104 ISSN 1070-6631, 1089-7666 URL `http://scitation.aip.org/content/aip/journal/pof2/21/1/10.1063/1.3054150`

[13] Hattori Y and Fukumoto Y 2014 *Journal of Fluid Mechanics* **738** 222–249 ISSN 1469-7645 URL `http://journals.cambridge.org/article_S0022112013005910`

[14] Felli M, Camussi R and Di Felice F 2011 *Journal of Fluid Mechanics* **682** 5–53 URL `http://journals.cambridge.org/abstract_S0022112011001509`

[15] Bolnot H 2012 *Instabilités des tourbillons hélicoïdaux: application au sillage des rotors* Thèse de doctorat Aix-Marseille Université France

[16] Bolnot H, Le Dizès S and Leweke T 2014 *Fluid Dyn. Res.* **46** 061405 ISSN 1873-7005 URL `http://stacks.iop.org/1873-7005/46/i=6/a=061405`

[17] Quaranta H U, Bolnot H and Leweke T 2015 *Journal of Fluid Mechanics* **780** 687–716 URL `http://journals.cambridge.org/abstract_S0022112015004796`

[18] Delbende I, Rossi M and Daube O 2012 *Theoretical and Computational Fluid Dynamics* **26** 141–160 ISSN 1432-2250 URL http://dx.doi.org/10.1007/s00162-011-0241-y

[19] Selçuk C 2016 *Numerical study of helical vortices and their instabilities* Thèse de doctorat Université Pierre et Marie Curie France

[20] Selçuk C, Delbende I and Rossi M *Submitted to Phys. Rev. Fluids*

[21] Carden R 2012 *Ritz values and Arnoldi convergence for non-Hermitian matrices* Thesis Rice University URL https://scholarship.rice.edu/handle/1911/70215

[22] Edwards W S, Tuckerman L S, Friesner R A and Sorensen D C 1994 *Journal of Computational Physics* **110** 82–102 ISSN 0021-9991 URL http://www.sciencedirect.com/science/article/pii/S0021999184710072

[23] Bagheri S, Schlatter P, Schmid P J and Henningson D S 2009 *Journal of Fluid Mechanics* **624** 33–44 ISSN 1469-7645, 0022-1120 URL https://www.cambridge.org/core/journals/journal-of-fluid-mechanics/article/global-stability-of-a-jet-in-crossflow/3777A4D80B58F23625EF95E5D7486B41

[24] von Kàrmàn T and Rubach H 1912 *Phys. Z* **13**

[25] Lamb H 1932 *Hydrodynamics* (Cambridge university press)

[26] Levy H and Forsdyke A G 1927 *Proceedings of the Royal Society of London. Series A, Containing Papers of a Mathematical and Physical Character* **114** 594–604 ISSN 0950-1207 URL http://www.jstor.org/stable/94831

[27] Abramowitz M and Stegun I 1965 *Handbook of Mathematical Functions* (Dover Publications)

[28] Widnall S E, Bliss D and Zalay A 1971 Theoretical and Experimental Study of the Stability of a Vortex Pair *Aircraft Wake Turbulence and Its Detection* ed Olsen J H, Goldburg A and Rogers M (Springer US) pp 305–338 ISBN 978-1-4684-8348-2 978-1-4684-8346-8 dOI: 10.1007/978-1-4684-8346-8_19 URL http://link.springer.com/chapter/10.1007/978-1-4684-8346-8_19

[29] Brancher P and Chomaz J M 1997 *Phys. Rev. Lett.* **78** 658–661 URL http://link.aps.org/doi/10.1103/PhysRevLett.78.658

[30] Meunier P, Ehrenstein U, Leweke T and Rossi M 2002 *Physics of Fluids* **14, n° 8** 2757–2766 10 p. URL https://hal.archives-ouvertes.fr/hal-00081683

[31] Josserand C and Rossi M 2007 *European Journal of Mechanics - B/Fluids* **26** 779–794 URL http://dx.doi.org/10.1016/j.euromechflu.2007.02.005

[32] Alfredsson P and Dahlberg J A 1979 A preliminary wind tunnel study of windmill wake dispersion in various flow conditions Tech. Rep. FFA TN AU-1499, Part 7(1) Aeronautical Research Institute of Sweden

[33] Sherry M, Nemes A, Lo Jacono D, Blackburn H M and Sheridan J 2013 *Physics of Fluids* **25** 117102 ISSN 10706631 URL `http://scitation.aip.org/content/aip/journal/pof2/25/11/10.1063/1.4824734`

[34] Delbende I, Piton B and Rossi M 2015 *European Journal of Mechanics - B/Fluids* **49, Part B** 363–372 ISSN 0997-7546 URL `http://www.sciencedirect.com/science/article/pii/S0997754614000570`

[35] Delbende I and Rossi M 2013 Dynamics of the three helical vortex system and instability *Proceedings of the International Conference on Aerodynamics of Offshore Wind Energy Systems and Wakes (ICOWES), Lyngby, Denmark* pp 224–235

[36] Leweke T, Bolnot H, Quaranta U and Le Dizès S 2013 Local and global pairing in helical vortex systems *Proceedings of the International Conference on Aerodynamics of Offshore Wind Energy Systems and Wakes (ICOWES), Lyngby, Denmark* pp 94–101